2026 IEEE International Conference on Robotics and Automation (ICRA 2026)
June 1-5, 2026. Vienna, Austria

A Centerline-Aligned Frenet Graph Framework for Surface-Based Path Planning in Pipeline Environments

Hao Liu[1], Gang Liu[2*], Chuan Qin[3], Yu Wang[2]

***Abstract*— Pipeline inspection is essential for maintaining the safety of critical infrastructure, but manual inspection is dangerous and inefficient, and existing robotic solutions struggle to handle curved and constrained surfaces. Traditional planning methods are either computationally expensive or prone to redundancy and discretization artifacts. To address these challenges, this paper proposes a centerline-aligned Frenet graph framework for surface-based path planning in pipeline environments. By embedding the pipeline surface into a structured two-dimensional manifold passing through the pipeline's central axis, the framework enables efficient heuristic search while maintaining geometric consistency. By combining quadratic programming with kinematic limits, an initial geodesic constrained path is generated and optimized, resulting in a smooth and executable trajectory. Extensive experiments on pipelines with sharp bends, intersections, and real-world pipeline environments demonstrate significant improvements in computational efficiency, path quality, and robustness compared to traditional methods.**

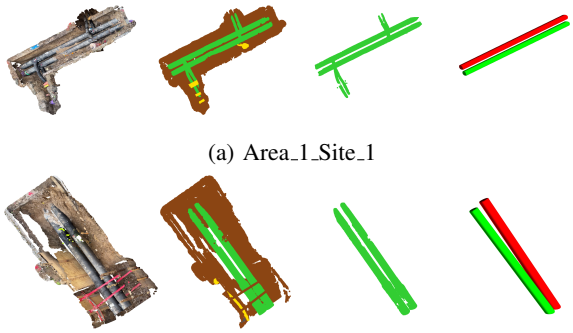

(a) Area_1_Site_1

(b) Area_1_Site_2

Fig. 1: Underground pipeline data from OpenTrench3D [9], processed by RANSAC algorithm to obtain a complete pipeline.

I. Introduction

Pipeline inspection robots have attracted considerable attention due to their potential to enhance safety and efficiency in the oil and gas industries. However, the interior pipeline environment presents formidable challenges. Narrow spaces, complex geometries, severe electromagnetic shielding, and unpredictable factors such as residual liquids, slippery surfaces, and harsh environmental conditions often make wired and wireless remote control impractical [1]. These difficulties highlight the necessity of autonomous navigation systems capable of ensuring reliable robot operation without human intervention [2].

Despite substantial progress in path planning for 2D planar and 3D free-space environments, existing approaches are generally unsuitable for climbing pipeline robots. These robots must traverse irregular two-dimensional manifolds with sharp curvature variations and strict geometric constraints [3]. The unique challenge lies in maintaining stable adhesion while adapting to twisted pipe surfaces, where improper path planning can cause detachment or falls. Hence, specialized path planning algorithms tailored to both the kinematic characteristics of climbing robots and the geometric complexity of pipelines are urgently needed [4].

In particular, magnetic wheeled robots, a common type of climbing robot, exhibit a motion behavior analogous to that of ground vehicles constrained to uneven two-dimensional manifolds [5]. For such robots, path quality is directly related to stability and safety: poorly planned paths risk slippage or rolling, while carefully optimized paths ensure adequate adhesion and mitigate hazards [6], [7]. This places strict requirements on the feasibility and computational efficiency of path planning algorithms, making the development of robust, geometry-aware methods essential for reliable pipeline inspection [8].

Industrial pipelines are typically composed of circular metal tubes with distinct geometric properties, including a central axis and a defined radius. These characteristics make pipelines a semistructured environment[10]. However, traditional 3D perception methods often struggle to accurately model the continuously changing curvature of the pipeline surface, especially at bends and junctions, leading to accumulated modeling errors and reducing the precision of Cartesian coordinate-based path planning. In contrast, using a model based on the central axis and radius of the pipeline provides a simpler and more accurate geometric representation, offering a more reliable foundation for path planning [11], [12].

This paper proposes a novel path planning framework for magnetic wheeled robots in pipeline environments. This framework parameterizes the two-dimensional manifold of the pipe using its central axis and efficiently discretizes it

This work was supported by the National Key R&D Program of China under Grant No. 2021YFA0716603

[1]The author is with the Lab for High Technology, Tsinghua University, Beijing, China liu_hao97@hotmail.com

[2]The authors are with the Department of Electronic Engineering, Tsinghua University, Beijing, China {liu_gang, yu-wang}@tsinghua.edu.cn

[3]The author is with the Institute for AI Industry Research, Tsinghua University, Beijing, China qincq1@student.unimelb.edu.au

*Corresponding author

using the Frenet coordinate system to create a structured mesh. An initial feasible path is generated using a heuristic search strategy based on the geodesic principle. The path is then optimized using a quadratic optimization procedure that incorporates the robot's kinematic constraints, ultimately yielding a smooth, safe, and executable trajectory. This framework significantly improves computational efficiency and path quality compared to traditional methods. Extensive simulation results validate the effectiveness and robustness of this approach in complex pipeline environments, demonstrating its potential for reliable real-world pipeline inspection applications.

We summarize our contributions as follows.

1) We propose a Frenet-aligned parametric manifold representation that embeds the pipeline surface into a two-dimensional parameter domain, ensuring analytically continuous normal fields and providing a high-fidelity yet computationally efficient basis for dimension-reduced path planning and control, significantly reducing representation and search complexity.

2) Within this Frenet framework, we introduce a more accurate surface path computation method, together with a set of geometric and physical metrics (e.g., arc length, curvature, support utilization, and energy consumption) and a unified optimization scheme, yielding smooth and energy-efficient executable trajectories.

3) We extensively validated the proposed method through simulations, ablation studies, and real-world experiments with a magnetic wheeled robot. Results in complex pipeline scenarios with sharp bends, junctions, and narrow segments demonstrate superior computational efficiency, path quality, and energy performance compared to baseline methods, highlighting its potential for industrial deployment.

II. Related Work

Path planning on curved and constrained surfaces has garnered considerable interest, particularly in applications involving wall-climbing and pipeline inspection robots. Early methods approached the problem through constrained optimization or mixed integer programming to ensure feasible climbing motions [8], [13]. While these approaches offer strong theoretical guarantees, they are computationally intensive and scale poorly to large environments. To mitigate this, some works integrated surface reconstruction from point clouds into planning frameworks [14], [15], [16]. However, such methods remain vulnerable to noise and irregularities in mesh quality.

Sampling-based planners provide a versatile framework for motion planning on nonplanar surfaces. Algorithms such as RRT* [17] and its informed variants [18] achieve asymptotic optimality, but their direct application to curved manifolds often results in high sampling inefficiency. Navigation mesh-based techniques [19] and vector-field methods on triangular meshes [20] alleviate this issue by embedding constraints directly into the surface representation. Nevertheless, these methods can be affected by discretization errors or high memory demands. Classical heuristic approaches, including enhanced A* algorithms [21] and Bézier curve smoothing [22], are effective for local path refinement but often lack global optimality guarantees. In pipeline environments, graph-based algorithms such as the advanced Dijkstra method have also been applied for automated 3D piping route design, demonstrating efficiency in structured tubular networks [23].

In the context of wall-climbing and in-pipe robots, path planning is inherently tied to adhesion and locomotion capabilities. Comprehensive reviews [24], [25] outline a variety of adhesion mechanisms, such as dry adhesives [26], electroadhesion [27], and magnetic systems [28]. While these studies address the mechanical aspects of surface traversal, few offer integrated solutions for efficient and reliable path planning. Some research has focused on autonomous navigation within unknown pipeline configurations, emphasizing reactive and perception-driven strategies [29]. Additionally, optimization-based path planning has been explored in applications such as welding complex joints, highlighting the need for computational efficiency in geometrically intricate settings [30].

Recent advances leverage geometric and skeleton-based representations to capture the intrinsic structure of 3D environments. Centerline extraction techniques for tubular structures [31] and digital skeletonization methods [32] provide compact and meaningful abstractions suitable for pipeline environments. However, their performance can degrade in the presence of surface noise or geometric irregularities. These approaches inspire our proposed centerline-aligned Frenet graph framework, which combines geometric coherence with computational efficiency to support robust and optimized path planning in pipeline settings.

III. Frenet-based Discretized Planning Grid

The position of a point in space is typically expressed as a linear combination of the standard basis vectors in a Cartesian coordinate system, whose basis consists of three mutually orthogonal unit vectors denoted by $\mathbf{e}_x$, $\mathbf{e}_y$, and $\mathbf{e}_z$. However, the Cartesian coordinate system cannot accurately represent the continuity of the pipe's two-dimensional manifold.

The Frenet coordinate system provides a local reference frame naturally aligned with the geometry of the pipeline. Let the spatial curve $\mathbf{c}(s)$ represent the centerline of the pipe, where $s \in [0, L]$ denotes the arc-length parameter. The associated Frenet frame consists of the tangent vector $\mathbf{T}(s)$, the principal normal vector $\mathbf{N}(s)$, and the binormal vector $\mathbf{B}(s)$, which satisfy the classical Frenet–Serret differential equations:

$$\begin{aligned} \frac{\mathrm{d}\mathbf{T}}{\mathrm{d}s} &= \kappa\,\mathbf{N}, \\ \frac{\mathrm{d}\mathbf{N}}{\mathrm{d}s} &= -\kappa\,\mathbf{T} + \tau\,\mathbf{B}, \\ \frac{\mathrm{d}\mathbf{B}}{\mathrm{d}s} &= -\tau\,\mathbf{N}. \end{aligned} \tag{1}$$

where $\kappa(s)$ and $\tau(s)$ denote the curvature and torsion of $\mathbf{c}(s)$, respectively, fully describing its local geometric properties.

This formulation not only defines a local reference frame along the centerline but also provides a precise mathematical description of the pipe manifold's geometry. By leveraging the Frenet–Serret equations, the curvature $\kappa(s)$ and torsion $\tau(s)$ fully characterize the intrinsic bending and twisting behavior of the spatial curve $\mathbf{c}(s)$, which are essential for capturing the geometric features of the pipeline surface. Consequently, the pipe manifold can be parameterized using the centerline and its associated Frenet frame, enabling an accurate and compact representation of the three-dimensional structure.

The pipe surface can then be regarded as a two-dimensional differentiable manifold $\mathcal{M}$ embedded in three-dimensional Euclidean space, with a standard representation defined by:

$$\mathcal{M} \subset \mathbb{R}^3, \dim(\mathcal{M}) = 2, \exists\, \mathbf{\Phi} : U \subset \mathbb{R}^2 \to \mathcal{M} \subset \mathbb{R}^3. \quad (2)$$

To formalize this representation, a local direction vector is defined within the normal plane at each point along the centerline as follows:

$$\boldsymbol{\omega}(s, \theta) = \cos\theta \mathbf{N}(s) + \sin\theta \mathbf{B}(s), \quad (3)$$

where θ denotes the rotational angle around the centerline, specifying a direction within the normal plane spanned by $\mathbf{N}(s)$ and $\mathbf{B}(s)$. The vector $\boldsymbol{\omega}(s, \theta)$ establishes a consistent local angular reference frame along the centerline.

The pipe surface can be parametrically represented as:

$$\mathbf{\Phi}(s, \theta) = \mathbf{c}(s) + \delta(s) \left[\cos\theta \mathbf{N}(s) + \sin\theta \mathbf{B}(s)\right]. \quad (4)$$

where $\delta(s)$ denotes the local radius of the pipe. This mapping projects the two-dimensional parameter domain (s, θ) onto a smooth surface embedded in three-dimensional Euclidean space. As shown in Fig. 2, the image defines a continuous tubular manifold that faithfully captures the geometry of the pipe surface along the centerline.

Based on the parametric surface formulation $\mathbf{\Phi}(s, \theta)$, the manifold $\mathcal{M}$ can be discretized by sampling the parameter domain $[0, L] \times [0, 2\pi)$ along the s and θ directions. These samples lie strictly on the manifold, eliminating the need for post-projection or surface reconstruction, and ensuring geometric accuracy and consistency.

Compared to conventional voxel grids or mesh-based reconstructions, the surface generated through this parametric mapping preserves geometric coherence, allows controllable sampling resolution, and retains a smooth and continuous normal vector field. These properties are particularly advantageous for motion planning on constrained surfaces. A path can be represented as a set of trajectory points mapped onto the manifold, i.e., $\mathbf{r} = \mathbf{\Phi}(s_i, \theta_i)_{i=1}^{N} \subset \mathcal{M}$, which enables planning to be conducted entirely within the surface space. This eliminates redundant degrees of freedom in Cartesian space and provides a structured foundation for trajectory optimization.

The normal vector $\boldsymbol{\omega}$ defined in the Frenet frame inherits the smooth geometric properties of the pipe centerline,

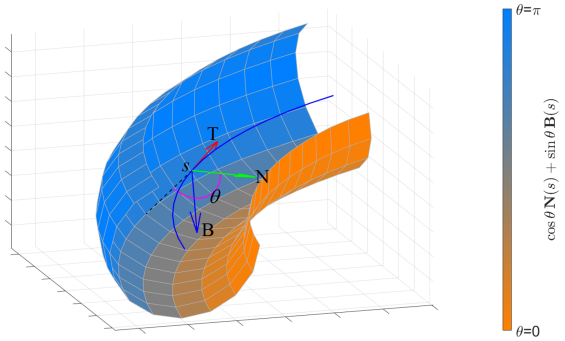

Fig. 2: Frenet coordinate system framework. The gradient color in the figure represents the change of the $\boldsymbol{\omega}(s, \theta)$ as θ changes.

offering significantly higher consistency than normal vectors estimated from discrete Cartesian samples. This continuous representation is particularly important for climbing robots that rely on stable multipoint contact and continuous surface attachment, as it helps reduce attitude tracking errors and improve trajectory stability.

Moreover, the Frenet grid supports strong local adaptability. In regions with high curvature, dense obstacles, or structural discontinuities, the discretization intervals Δs and $\Delta\theta$ can be refined to generate locally denser meshes. Path reconstruction can then be performed efficiently on subgrids. If a local obstacle region Ω is detected, it can be mapped to a subdomain $\Omega_{s\theta}$ in the (s, θ) space, enabling rapid local obstacle avoidance without modifying the global path structure. This capability is particularly valuable for real-time pipeline inspection and maintenance tasks.

IV. Geometric and Physical Metrics

To evaluate the feasibility and efficiency of a surface path for climbing robots, we define three core metrics: arc length, smoothness, and energy consumption. These metrics jointly capture the geometric regularity and physical effort required for stable locomotion on curved surfaces.

A. Arc length

To investigate the geometric properties of parametric curves on a surface, we consider the arc length between two path points $\mathbf{r}(s_a, \theta_a)$ and $\mathbf{r}(s_b, \theta_b)$. The arc length $\mathbf{L}_{ab}$ is defined as the integral of the norm of the derivative of the position vector along the path over the interval $[a, b]$:

$$\mathbf{L}_{ab} = \int_{s_a}^{s_b} \left\| \frac{\partial \mathbf{r}}{\partial s} \right\| ds \quad (5)$$

Here, $\left\| \frac{\partial \mathbf{r}}{\partial s} \right\|$ represents the magnitude of the tangent vector to the path at each point. This quantity measures how the position vector changes along the curve as s varies.

The coefficients E, F, and G of the first fundamental form describe the inner products between surface tangent vectors, thereby defining how local distances are measured on the parameterized surface. These coefficients are derived

from the partial derivatives of the position vector $\mathbf{r}(s,\theta)$ with respect to the parameters s and θ, and are given by:

$$E = \left\langle \frac{\partial \mathbf{r}}{\partial s}, \frac{\partial \mathbf{r}}{\partial s} \right\rangle, F = \left\langle \frac{\partial \mathbf{r}}{\partial s}, \frac{\partial \mathbf{r}}{\partial \theta} \right\rangle, G = \left\langle \frac{\partial \mathbf{r}}{\partial \theta}, \frac{\partial \mathbf{r}}{\partial \theta} \right\rangle \quad (6)$$

These coefficients E, F, and G allow us to compute the arc length by incorporating the local geometry of the surface. Specifically, for a parameterized curve on the surface described by $(s(t),\theta(t))$, the arc length formula can be rewritten in terms of these coefficients as:

$$\mathbf{L}_{ab} = \int_a^b \sqrt{E\left(\frac{ds}{dt}\right)^2 + 2F\frac{ds}{dt}\frac{d\theta}{dt} + G\left(\frac{d\theta}{dt}\right)^2}\, dt \quad (7)$$

To expand the derivative $\frac{d\mathbf{r}}{dt}$, its partial derivatives with respect to the parameters s and θ are considered. The partial derivative of $\mathbf{r}$ with respect to s is expressed as:

$$\frac{\partial \mathbf{r}}{\partial s} = \mathbf{T}(s) + \delta'(s)\,\boldsymbol{\omega}(s,\theta) + \delta(s)\frac{d\boldsymbol{\omega}}{ds} \quad (8)$$

According to 2, we get the derivatives of $\mathbf{B}(s)$ and $\mathbf{N}(s)$:

$$\begin{aligned} \mathbf{N}'(s) &= -\kappa(s)\mathbf{T}(s) + \tau(s)\mathbf{B}(s), \\ \mathbf{B}'(s) &= -\tau(s)\mathbf{N}(s). \end{aligned} \quad (9)$$

The derivative of $\boldsymbol{\omega}(s,\theta)$ with respect to s can be written as:

$$\frac{d\boldsymbol{\omega}}{ds} = -\kappa\cos\theta\,\mathbf{T} + \tau\cos\theta\,\mathbf{B} - \tau\sin\theta\,\mathbf{N}. \quad (10)$$

Hence the complete form of the partial derivative becomes:

$$\begin{aligned} \frac{\partial \mathbf{r}}{\partial s} &= (1-\delta(s)\kappa(s)\cos\theta)\,\mathbf{T}(s) + \delta'(s)\,\boldsymbol{\omega}(s,\theta) \\ &\quad + \delta(s)\tau(s)\,(\cos\theta\,\mathbf{B}(s) - \sin\theta\,\mathbf{N}(s)) \end{aligned} \quad (11)$$

The partial derivative of $\mathbf{r}$ with respect to θ is:

$$\frac{\partial \mathbf{r}}{\partial \theta} = \delta(s)(\cos\theta\,\mathbf{B}(s) - \sin\theta\,\mathbf{N}(s)) \quad (12)$$

The first fundamental form coefficients E, F, and G describe the inner products between surface tangent vectors and define how local distances are measured on the parameterized surface. Based on the previously derived expressions for the partial derivatives, these coefficients are computed as:

$$\begin{aligned} E &= \left\langle \frac{\partial \mathbf{r}}{\partial s}, \frac{\partial \mathbf{r}}{\partial s} \right\rangle = \\ &(1-\delta(s)\kappa(s)\cos\theta)^2 + (\delta'(s))^2 + (\delta(s)\tau(s))^2, \\ F &= \left\langle \frac{\partial \mathbf{r}}{\partial s}, \frac{\partial \mathbf{r}}{\partial \theta} \right\rangle = \delta^2(s)\tau(s), \\ G &= \left\langle \frac{\partial \mathbf{r}}{\partial \theta}, \frac{\partial \mathbf{r}}{\partial \theta} \right\rangle = \delta^2(s). \end{aligned} \quad (13)$$

It is noted that $\mathbf{T}$, $\boldsymbol{\omega}$, and $\cos\theta\,\mathbf{B} - \sin\theta\,\mathbf{N}$ are mutually orthogonal, which facilitates previous calculations.

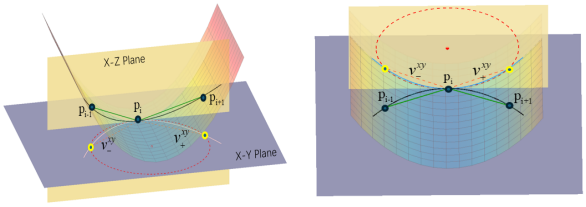

(a) κ_{xy} (b) κ_{xz}

Fig. 3: Projection of path points in the vehicle body coordinate system and calculation of curvature.

B. Smoothness

Consider a path point on the surface of the pipe, whose parameters are $\mathbf{p}(s_i,\theta_i)$. The surface normal vector of this point is:

$$\mathbf{n}(s_i,\theta_i) = -\boldsymbol{\omega}(s_i,\theta_i) \quad (14)$$

As shown in fig. 3, the two adjacent points of point $\mathbf{p}_{i\pm1}$ can be expressed as:

$$\mathbf{p}_{i\pm1} = \mathbf{P}(s_{i\pm1},\theta_{i\pm1}) \quad (15)$$

Based on three path points and the normal vector, we can obtain two projected vectors lying on the normal plane, which is also the xy plane of the robot:

$$\mathbf{v}_{\pm}^{xy} = \left(\mathbf{I} - \mathbf{n}_i\mathbf{n}_i^{\mathrm{T}}\right)(\mathbf{p}_{i\pm1} - \mathbf{p}_i) \quad (16)$$

The cosine of the angle between these projected vectors is computed as:

$$\cos(s,\theta) = \frac{\mathbf{v}_-^{xy}\cdot\mathbf{v}_+^{xy}}{\left\|\mathbf{v}_-^{xy}\right\|\left\|\mathbf{v}_+^{xy}\right\|} \quad (17)$$

The curvature at the path point is then estimated using the three-point circumcircle approximation:

$$\kappa_{xy}(s,\theta) = \frac{2\sin(s,\theta)}{\left\|\mathbf{v}_+^{xy} - \mathbf{v}_-^{xy}\right\|} \quad (18)$$

Following the same curvature estimation procedure, the curvature κ_{xz} in the xz-plane can be derived, which characterizes the bending degree of the robot's climbing path in the lateral plane.

C. Energy consumption

The adhesion force required to stabilize the robot's motion results in energy consumption. The passive normal reaction of the wall does not perform mechanical work, but it reduces the active adhesion needed to counteract gravity. This reduction is characterized by the support utilization index c_i, which is defined as:

$$c_i = \max(0,\ -\hat{\mathbf{g}}\cdot\mathbf{n}_i), \quad c_i \in [0,1] \quad (19)$$

where $\mathbf{n}_i$ is the contact normal, and $\hat{\mathbf{g}}$ is the unit gravity vector. A higher c_i indicates stronger passive support. The active gripping force F_{grip} needed at position (s_i,θ_i) is given by:

$$F_{\text{grip}} = mg(1-c_i) \quad (20)$$

The path-average support utilization $\bar{c} = \frac{1}{N}\sum c_i$ is an important indicator of overall support efficiency, and the corresponding mean adhesion demand is:

$$\bar{F}_{\text{grip}} = mg(1 - \bar{c}) \tag{21}$$

Although the support itself does not generate work, maintaining F_{grip} consumes energy, which is modeled as:

$$\mathcal{E}_{\text{adh}}(s_i, \theta_i) = \left(F_{\text{grip}}\right)^2 \tag{22}$$

emphasizing the nonlinear increase of power with adhesion force. In addition, the drive system must perform positive tangential work to overcome uphill gravity and rolling resistance,

$$\Delta\mathcal{E}_{\text{drive}}(i) = \max\left(0, -mg\left(\hat{\mathbf{g}} \cdot \mathbf{t}_i\right)\right)\Delta s + \mu_r mg\Delta s \tag{23}$$

where $\mathbf{t}_i$ is the tangential force, and μ_r is the rolling resistance coefficient. The total energy consumed by the drive system along the trajectory is given by $\mathcal{E}_{\text{drive}}$.

Thus, the total energy consumption is the sum of the adhesion-related energy and the drive energy:

$$\mathcal{E}_{\text{total}} = \sum_i \mathcal{E}_{\text{adh}}(s_i, \theta_i) + \mathcal{E}_{\text{drive}} \tag{24}$$

which clearly separates adhesion costs from mechanical traction work. This formulation shows that paths with higher support utilization $\bar{c}$ require less adhesion and, therefore, reduce overall energy expenditure.

V. Path Search and Optimization

A. Initial path search

Constructing a discrete grid based on the Frenet coordinate system is a key strategy in this work to balance path planning accuracy with dynamic adaptability, and accordingly, the planning algorithm must be suitably adapted. Unlike traditional Cartesian grid search, the robot state in the Frenet framework is defined as (s, θ, ψ), where ψ denotes the robot's heading angle on local surface. To ensure motion feasibility, state transitions are governed by an incomplete motion model. Given control inputs linear velocity v and steering angle ϕ, the state trajectory is generated by a hybrid A* planner. In the Frenet space, state propagation is no longer performed through Euclidean forward simulation in (x, y, θ) space, but is instead directly carried out in the parameter space (s, θ, ψ). On this basis, we employ the hybrid A* algorithm to generate the initial path, as its inherent angular constraints ensure that the resulting trajectory complies with the robot's steering limitations, thereby improving both the feasibility and physical realizability of the initial solution.

B. Path optimization

We formulate a path refinement process based on constrained optimization and an initial path. A unified objective function is constructed to jointly minimize three criteria: path length, smoothness, and energy consumption. The optimization variables are defined as the Frenet parameters of discrete path points:

$$\mathbf{x} = [s_1, \theta_1, s_2, \theta_2, \ldots, s_n, \theta_n]^T \tag{25}$$

The overall objective adopts a weighted-sum formulation:

$$\min_{\mathbf{x}} f(\mathbf{x}) = w_1\mathcal{H}_{\text{length}} + w_2\mathcal{H}_{\text{smooth}} + w_3\mathcal{H}_{\text{energy}} \tag{26}$$

where w_1, w_2, and w_3 are the relative weights of each cost component. The specific definitions of the three sub-objectives are:

$$\begin{aligned} \mathcal{H}_{\text{length}} &= \sum_{i=1}^{n-1} \left\|\mathbf{r}(s_{i+1}, \theta_{i+1}) - \mathbf{r}(s_i, \theta_i)\right\|^2, \\ \mathcal{H}_{\text{smooth}} &= \sum_{i=2}^{n-1} \kappa_i^2, \\ \mathcal{H}_{\text{energy}} &= \sum_{i=1}^{n} \mathcal{E}(s_i, \theta_i)^2. \end{aligned} \tag{27}$$

The optimization is subject to the following constraints:

Position constraints:

$$\begin{aligned} s^{\text{ref}} - s_l \le s_i \le s^{\text{ref}} + s_u, \\ \theta^{\text{ref}} - \theta_l \le \theta_i \le \theta^{\text{ref}} + \theta_u. \end{aligned} \tag{28}$$

Geometric constraint: All path points lie on the pipe surface, which is inherently satisfied by the Frenet-based parameterization.

Obstacle avoidance constraint: Path points must lie outside obstacle regions, $\mathbf{r}(s_i, \theta_i) \notin \Omega$, or equivalently $(s_i, \theta_i) \notin \Omega_{s,\theta}$ in the parameter space.

Curvature constraint: Local curvature must satisfy $\kappa_i \le \kappa_{\max}$ to ensure smooth and physically feasible motion.

Boundary conditions:

$$\mathbf{r}(s_1, \theta_1) = \mathbf{r}_{\text{start}}, \quad \mathbf{r}(s_n, \theta_n) = \mathbf{r}_{\text{end}}. \tag{29}$$

The optimization problem can be solved using IPOPT, which is a powerful solver for large-scale nonlinear optimization problems. IPOPT is particularly well-suited for this kind of problem, where the objective function is smooth and quadratic, and the constraints are non-linear (such as curvature and obstacle avoidance). By providing an initial guess for the path and setting the weights w_1, w_2, and w_3, IPOPT can iteratively refine the path to meet the desired objectives while satisfying the constraints.

VI. Performance Evaluation

To validate the proposed path planning method for magnetic wheeled robots based on the Frenet coordinate system, we conducted both simulation and real-world experiments. The simulation covered various pipeline configurations, including straight segments, high curvature bends, and multi-branch junctions, reflecting diverse operational conditions. The robot's kinematic model and control parameters were consistent across all experiments for comparability.

Simulations were performed on a ROS and Gazebo platform, with pipeline scenarios modeled in Blender.

TABLE I: Scenario parameters

Scenario	$l \times w \times h$ (m)	Points	Resolution (m)
Spiral*	$4.0 \times 2.52 \times 6.80$	100034	0.02
Pipe Network*	$16.0 \times 0.52 \times 10.26$	174196	0.02
Area_1_Site_1†	$8.17 \times 4.57 \times 0.42$	106810	0.01
Area_1_Site_2†	$4.77 \times 6.20 \times 0.45$	96252	0.01

* Synthetic models developed in our simulation system.
† Real-world scenes from the OpenTrench dataset.

The OpenTrench dataset [9], a real-world underground pipeline benchmark, is also employed for algorithmic validation. This dataset provides high precision 3D point clouds of representative underground tubular structures, which were used to construct the testing environment. Centerlines can be reliably extracted from point clouds by some methods [8], [13]. In this paper. we use the RANSAC algorithm to extract the centerline and reconstruct pipeline models for testing. An example is shown in Fig. 1, with pipeline parameters summarized in Table I.

A magnetic wheeled robot with dimensions 30 × 20 × 20 cm and equipped with a Livox Mid-360 LiDAR was used for physical validation. Its chassis design allows stable complex maneuvers within ferromagnetic pipelines.

Evaluation metrics included path length, path curvature κ_{xy} and κ_{xz}, as well as total energy consumption $\mathcal{E}_{\text{total}}$ to assess trajectory efficiency and feasibility.

A. Ablation study

To evaluate the effectiveness of the proposed Frenet based framework, an ablation study was conducted by systematically replacing its search and optimization modules with Cartesian coordinates. The results summarized in Table II, demonstrate clear advantages of the Frenet approach in path planning quality and energy efficiency.

The Cartesian baseline path is the longest, at 96.5 meters. This is due to a mismatch between the path length searched based on Cartesian coordinates and the true path length. Furthermore, κ_{xy}^{max} and κ_{xz}^{max} are significantly excessive, indicating poor geometric conformance and unstable motion. In contrast, the Frenet based search shortens the path length to 89.2 meters and reduces energy consumption to 216 J, but the maximum curvature does not significantly decrease, and there is a poor balance between the κ_{xy}^{avg} and κ_{xz}^{avg}.

Using Frenet search and Frenet optimization, while the path length is longer, energy consumption is further reduced to 275 J, the maximum curvature is significantly reduced, and a good balance is achieved between the κ_{xy}^{avg} and κ_{xz}^{avg}.

Ablation studies confirm that the two Frenet based modules synergistically improve performance. The proposed framework consistently generates shorter, smoother, and more energy efficient paths, demonstrating its effectiveness in reliable pipeline inspection applications.

B. Comparative study

To evaluate the performance of the proposed Frenet based optimization method, a comparative study was conducted against three established baseline approaches: Stumm's method [15], Li's method [8], and Zhang's method [33]. All methods were implemented under identical conditions using a Frenet frame discretization grid, with each experiment repeated ten times to ensure statistical reliability. The evaluation metrics included path length, curvature in both horizontal and vertical planes, and total energy consumption, as summarized in Table III.

TABLE II: Performance of different modules.

Method	len (m)	κ_{xy}		κ_{xz}		$\mathcal{E}_{\text{total}}$ (J)
		avg	max	avg	max	
Cartesian	96.5	1.63	7.21	2.43	8.31	318
Frenet	85.4	1.15	5.78	1.89	7.48	275
Frenet+Opt	89.2	1.27	2.33	1.53	4.78	216

TABLE III: Performance of different algorithms.

Scenario	Method	len	κ_{xy}^{avg}	κ_{xz}^{avg}	$\mathcal{E}_{\text{total}}$ (J)
Spiral	Stumm's	23.3	0.92	1.76	39
	Li's	23.7	0.97	1.56	53
	Zhang's	23.0	1.11	1.84	51
	Ours	24.1	1.03	1.33	36
Pipe network	Stumm's	18.7	0.41	0.44	64
	Li's	18.1	0.59	0.22	61
	Zhang's	19.2	0.34	0.41	72
	Ours	17.5	0.31	0.12	57
Area_1_Site_1	Stumm's	6.4	0.51	0.13	24
	Li's	6.8	0.37	0.27	31
	Zhang's	5.9	0.34	0.21	27
	Ours	6.4	0.25	0.16	21
Area_1_Site_2	Stumm's	5.8	0.13	0.22	12
	Li's	5.3	0.07	0.17	13
	Zhang's	5.7	0.08	0.11	15
	Ours	5.5	0.10	0.07	9

In the spiral pipeline scenario, the proposed method achieved a significantly lower energy consumption of 36 J while maintaining a path length comparable to the baselines. This result demonstrates the method's ability to generate efficient trajectories with minimal unnecessary motion. Among the baselines, Stumm's and Li's methods produced smoother paths but at higher energy costs, while Zhang's method exhibited higher curvature values, leading to increased energy demand.

The pipe network scenario further highlighted the advantages of the proposed approach. It produced the shortest path at 17.5 meters and the lowest energy consumption of 57 J, effectively handling the complex junctions and directional changes. In contrast, the baseline methods either generated longer paths or higher curvature variations, resulting in reduced overall efficiency.

The experiments in Area_1_Site_1 and Area_1_Site_2 confirmed the consistency of the proposed method. In both environments, it achieved the lowest energy consumption values of 21 J and 9 J, respectively, while maintaining stable curvature profiles. These results indicate robust performance across both geometrically complex and relatively simple settings.

Overall, the proposed Frenet based optimization method

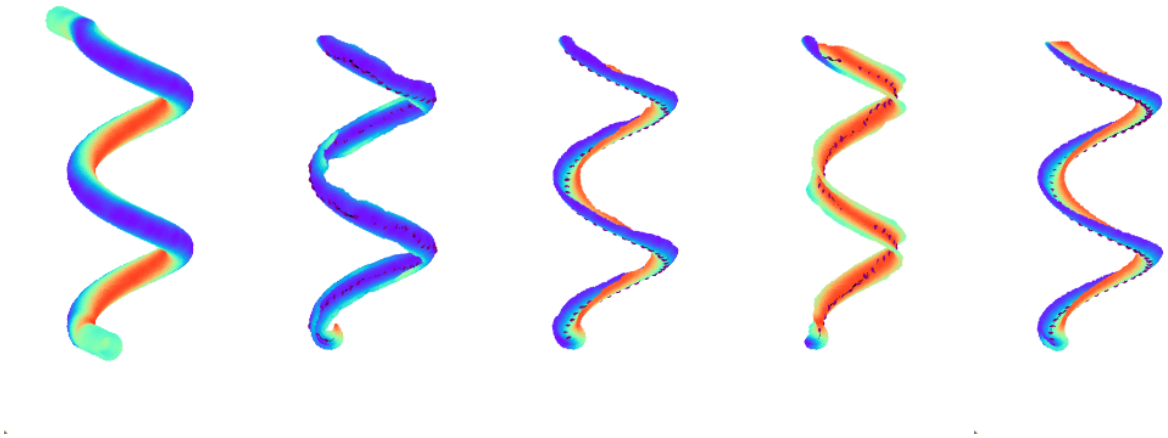

(a) Original pipe model (b) Stuum's (c) Li's (d) Zhang's (e) Ours

Fig. 4: Path comparison in complex pipeline scenarios.

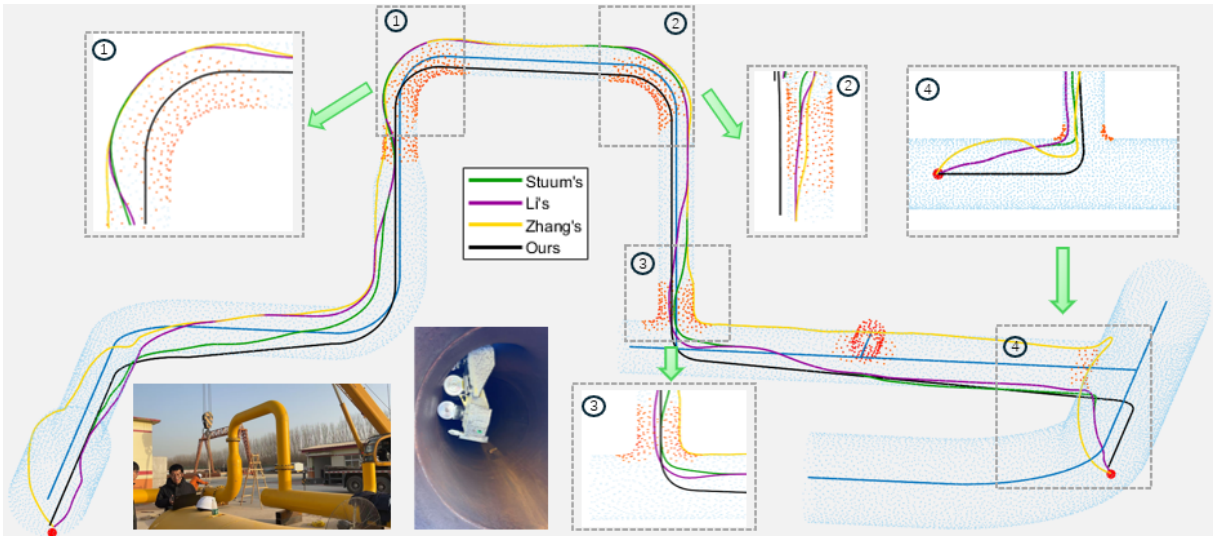

Fig. 5: Field experiment with a magnetic wheeled robot in a pipeline corridor containing sharp bends and narrow joints.

demonstrates superior performance in balancing path length, curvature smoothness, and energy efficiency. Its particularly strong performance in complex pipeline environments suggests substantial potential for practical applications in real-world inspection tasks.

C. Real-world experiments

To validate the applicability of the proposed approach in real-world scenarios, we conducted field experiments on a magnetic wheeled robot platform. As shown in Fig. 5, the test environment consisted of a complex pipeline corridor with multiple sharp bends and junctions. The minimum diameter of the pipe was only 50 cm, which substantially increased the risk of wall collisions. Under these challenging conditions, the proposed planner enabled the robot to maintain stable adhesion and successfully negotiate narrow turns without manual intervention. These results demonstrate the effectiveness and robustness of our method in realistic and highly constrained pipeline inspection tasks.

VII. Conclusion

This paper presented a path planning framework for magnetic wheeled robots for autonomous inspection inside pipelines. By utilizing the pipeline's geometric features, including its central axis and radius, and applying a Frenet coordinate-based representation, the method enables efficient modeling of the two-dimensional manifold of the pipeline surface. Experimental results demonstrate that the Frenet coordinate system outperforms the Cartesian coordinate system in terms of geometric adaptability, computational efficiency, and adhesion stability, especially in complex geometries such as curved and branched pipelines. Its parameterized representation significantly reduces computational complexity and improves path adherence. The proposed quadratic programming optimization further enhances path smoothness and reduces energy consumption compared to traditional

methods, better meeting the high precision path planning requirements for magnetic wheeled robots operating on the inner surface of pipelines and showing promising engineering application potential. Future work may focus on integrating more efficient centerline extraction methods and accelerated quadratic programming solvers to further improve overall system performance.

REFERENCES

[1] S. Gao, R. Hou, J. Li, Y. Pan, S. He, and H. Li, "Magnetic field analysis and structure design of a new magnetic wheel for wall-climbing robot," *Journal of Superconductivity and Novel Magnetism*, vol. 35, no. 2, pp. 529–537, 2022.

[2] K. Wu, "A survey on wireless in-pipe inspection robotics," *International Journal of Intelligent Robotics and Applications*, vol. 8, no. 3, pp. 648–670, 2024.

[3] Y. Fang, S. Wang, Q. Bi, D. Cui, and C. Yan, "Design and technical development of wall-climbing robots: A review," *Journal of Bionic Engineering*, vol. 19, no. 4, pp. 877–901, 2022.

[4] R. S. Elankavi, D. Dinakaran, A. S. A. Doss, R. K. Chetty, and M. Ramya, "Design and motion planning of a wheeled type pipeline inspection robot," *Journal of Robotics and Control (JRC)*, vol. 3, no. 4, pp. 415–430, 2022.

[5] W. Xu, C. Hou, G. Li, and C. Cui, "Path planning for wall-climbing robots using an improved sparrow search algorithm," in *Actuators*, vol. 13, no. 9. MDPI, 2024, p. 370.

[6] J. Zhang, X. Lin, and D. W. Hong, "Transition motion planning for multi-limbed vertical climbing robots using complementarity constraints," in *2021 IEEE International Conference on Robotics and Automation (ICRA)*. IEEE, 2021, pp. 2033–2039.

[7] X. Li, Y. Yang, Y. Yuan, Y. Ma, Y. Huang, and H. Ni, "Intelligent vehicle classification system based on deep learning and multisensor fusion," in *Fifth International Conference on Computer Vision and Data Mining (ICCVDM 2024)*, M. Yin and X. Zhang, Eds., vol. 13272, International Society for Optics and Photonics. SPIE, 2024, p. 1327228. [Online]. Available: https://doi.org/10.1117/12.3048375

[8] H. Li, J. Liao, S. Zhu, H. Ge, W. Song, X. Chen, and J. Gu, "Constrained path planning on pipeline surface for wall climbing robots," in *2022 IEEE International Conference on Robotics and Biomimetics (ROBIO)*. IEEE, 2022, pp. 1615–1622.

[9] L. H. Hansen, S. B. Jensen, M. P. Philipsen, A. Møgelmose, L. Bodum, and T. B. Moeslund, "Opentrench3d: a photogrammetric 3d point cloud dataset for semantic segmentation of underground utilities," in *Proceedings of the IEEE/CVF Conference on Computer Vision and Pattern Recognition*, 2024, pp. 7646–7655.

[10] W. Zhao, Z. Azizul, X. Lyu, and W. Kuang, "Information guided levy flight for robot search in unknown environments," *Journal of King Saud University Computer and Information Sciences*, 2026.

[11] J. Huang, Z. He, Y. Arakawa, and B. Dawton, "Trajectory planning in frenet frame via multi-objective optimization," *IEEE Access*, vol. 11, pp. 70 764–70 777, 2023.

[12] W. Zhao, Z. H. Azizul, C. S. Woo, W. Kuang, and Y. Li, "Potential-driven multi-learning particle swarm optimisation," *Swarm and Evolutionary Computation*, vol. 96, p. 101993, 2025.

[13] R. Yue, J. Xiao, S. Wang, and S. L. Joseph, "Three-dimensional path planning of a climbing robot using mixed integer linear programming," *Advanced Robotics*, vol. 24, no. 15, pp. 2087–2118, 2010.

[14] A. Breitenmoser and R. Siegwart, "Surface reconstruction and path planning for industrial inspection with a climbing robot," in *2012 2nd International Conference on Applied Robotics for the Power Industry (CARPI)*. IEEE, 2012, pp. 22–27.

[15] E. Stumm, A. Breitenmoser, F. Pomerleau, C. Pradalier, and R. Siegwart, "Tensor-voting-based navigation for robotic inspection of 3d surfaces using lidar point clouds," *The International Journal of Robotics Research*, vol. 31, no. 12, pp. 1465–1488, 2012.

[16] S. Yan, Y. Wang, K. Zhao, P. Shi, Z. Zhao, Y. Zhang, and J. Li, "Hemora: Unsupervised heuristic consensus sampling for robust point cloud registration," in *Proceedings of the Computer Vision and Pattern Recognition Conference*, 2025, pp. 1363–1373.

[17] S. Karaman and E. Frazzoli, "Sampling-based algorithms for optimal motion planning," *The International Journal of Robotics Research*, vol. 30, no. 7, pp. 846–894, 2011.

[18] J. D. Gammell, S. S. Srinivasa, and T. D. Barfoot, "Informed rrt*: Optimal sampling-based path planning focused via direct sampling of an admissible ellipsoidal heuristic," in *2014 IEEE/RSJ international conference on intelligent robots and systems*. IEEE, 2014, pp. 2997–3004.

[19] S. Pütz, T. Wiemann, J. Sprickerhof, and J. Hertzberg, "3d navigation mesh generation for path planning in uneven terrain," *IFAC-PapersOnLine*, vol. 49, no. 15, pp. 212–217, 2016.

[20] S. Pütz, T. Wiemann, M. K. Piening, and J. Hertzberg, "Continuous shortest path vector field navigation on 3d triangular meshes for mobile robots," in *2021 IEEE International Conference on Robotics and Automation (ICRA)*. IEEE, 2021, pp. 2256–2263.

[21] B. Li, C. Dong, Q. Chen, Y. Mu, Z. Fan, Q. Wang, and X. Chen, "Path planning of mobile robots based on an improved a* algorithm," in *Proceedings of the 2020 4th High Performance Computing and Cluster Technologies Conference & 2020 3rd International Conference on Big Data and Artificial Intelligence*, 2020, pp. 49–53.

[22] J.-w. Choi, R. Curry, and G. Elkaim, "Path planning based on bézier curve for autonomous ground vehicles," in *Advances in Electrical and Electronics Engineering-IAENG Special Edition of the World Congress on Engineering and Computer Science 2008*. IEEE, 2008, pp. 158–166.

[23] S.-W. Choi and E.-B. Lee, "Application of an advanced dijkstra algorithm for automation systems of 3d piping routing," in *2024 8th International Conference on Communication and Information Systems (ICCIS)*. IEEE, 2024, pp. 213–217.

[24] B. Chu, K. Jung, C.-S. Han, and D. Hong, "A survey of climbing robots: Locomotion and adhesion," *International journal of precision engineering and manufacturing*, vol. 11, pp. 633–647, 2010.

[25] A. Hajeer, L. Chen, and E. Hu, "Review of classification for wall climbing robots for industrial inspection applications," in *2020 IEEE 16th International Conference on Automation Science and Engineering (CASE)*. IEEE, 2020, pp. 1421–1426.

[26] M. P. Murphy and M. Sitti, "Waalbot: An agile small-scale wall-climbing robot utilizing dry elastomer adhesives," *IEEE/ASME transactions on Mechatronics*, vol. 12, no. 3, pp. 330–338, 2007.

[27] H. Prahlad, R. Pelrine, S. Stanford, J. Marlow, and R. Kornbluh, "Electroadhesive robots—wall climbing robots enabled by a novel, robust, and electrically controllable adhesion technology," in *2008 IEEE international conference on robotics and automation*. IEEE, 2008, pp. 3028–3033.

[28] J. Hu, X. Han, Y. Tao, and S. Feng, "A magnetic crawler wall-climbing robot with capacity of high payload on the convex surface," *Robotics and Autonomous Systems*, vol. 148, p. 103907, 2022.

[29] D.-H. Lee, H. Moon, and H. R. Choi, "Autonomous navigation of in-pipe working robot in unknown pipeline environment," in *2011 IEEE International Conference on Robotics and Automation*. IEEE, 2011, pp. 1559–1564.

[30] H. Fang, S. Ong, and A. Nee, "Robot path planning optimization for welding complex joints," *The International Journal of Advanced Manufacturing Technology*, vol. 90, no. 9, pp. 3829–3839, 2017.

[31] B. Kerautret, A. Krähenbühl, I. Debled-Rennesson, and J.-O. Lachaud, "3d geometric analysis of tubular objects based on surface normal accumulation," in *Image Analysis and Processing—ICIAP 2015: 18th International Conference, Genoa, Italy, September 7-11, 2015, Proceedings, Part I 18*. Springer, 2015, pp. 319–331.

[32] N. Karmakar, S. Mondal, and A. Biswas, "Determination of 3d curve skeleton of a digital object," *Information Sciences*, vol. 499, pp. 84–101, 2019.

[33] L. Zhang, J. Cao, B. Han, Z. Teng, Y. Cheng, K. Wang, and Q. Hao, "Effective trajectory generation for robots on general 3d curved surface," *IEEE Robotics and Automation Letters*, 2024.